JOURNAL OF CATALYSIS **167,** 234–241 (1997)
ARTICLE NO. CA971571

The CO + NO Reaction over Pd: A Combined Study Using Single-Crystal, Planar-Model-Supported, and High-Surface-Area Pd/Al_2O_3 Catalysts

D. R. Rainer, S. M. Vesecky, M. Koranne, W. S. Oh, and D. W. Goodman

Department of Chemistry, Texas A&M University, College Station, Texas 77843-3255

Received September 4, 1996; revised December 12, 1996; accepted December 13, 1996

A kinetics study of the CO + NO reaction over Pd has been carried out using single-crystal, model planar-supported, and conventional high-surface-area Pd/Al_2O_3 catalysts. A pronounced structure sensitivity is evident that results in a rate enhancement over the Pd(111) single crystal relative to the more open (100) and (110) faces, and for larger supported particles relative to smaller ones. Temperature-programmed desorption (TPD) and X-ray photoelectron spectroscopy (XPS) data indicate that the Pd(100) face is more active for NO dissociation and atomic N stabilization than the close-packed (111) plane. Similarly, TPD results show that smaller particles in the model supported catalysts are more active for atomic N formation and stabilization. The inverse correlation between reaction activity and N_a formation and stabilization suggests that an inactive atomic N species plays a role in determining the reaction rate. © 1997 Academic Press

I. INTRODUCTION

The CO + NO reaction has been studied over a variety of transition and noble metal catalysts (1–12). Since the introduction in the late 1970s of the three-way catalytic converter (for the simultaneous reduction of NO_x species and oxidation of CO and excess hydrocarbons) into the emission control systems of automobiles in the United States, there have been significant efforts to elucidate the fundamental reaction pathways and catalytic characteristics that account for the success of these systems (11–13). At the same time there has been an understandable desire to replace rhodium, the critical component in the Pt/Rh (90/10) catalysts currently predominantly used, with a cheaper, more plentiful substitute (13). As these types of pollution control measures are more widely adopted internationally, along with the increasing number of automobiles in operation, the desire to identify a Rh substitute becomes even more compelling. Palladium is one possible alternative; not only is it more plentiful, but it has also been found to be more durable at higher reaction temperatures. Thus a catalytic converter utilizing a Pd-only catalyst can be positioned nearer the engine than a Pt–Rh catalyst. Also, Pd has demonstrated excellent hydrocarbon oxidation characteristics, which becomes increasingly important as emissions control standards for unburnt hydrocarbons in this country are raised (14, 15).

Because the highly dispersed metal particles supported on high-surface-area insulating materials that comprise a substantial percentage of industrially applied heterogeneous catalysts are not amenable to study using typical UHV-based surface science probes, a common approach has been to simulate the kinetics of these systems using metal single-crystal model catalysts. Single crystals provide well-defined surface geometries and allow for a detailed atomic level characterization of the post reaction and adsorbate covered surface to be performed. These types of studies have been very successful in unambiguously relating catalytic behavior with specific crystal planes, in addition to providing information regarding the identity and role of certain promoters, inhibitors, and reaction intermediates (16–19).

However, there are also certain important issues associated with supported catalysts, such as intrinsic particle size effects and the role of the support, that single crystals by their nature obviously cannot address. The employment of planar-model-supported catalysts, prepared in UHV by evaporation of the metal of catalytic interest onto an oxide thin film (20–22), is an approach that features many of the advantages associated with single-crystal studies (i.e., suitability for UHV surface science study), while still undertaking to investigate the effect of particle size and the metal-support interaction. Additionally, these types of models allow for much tighter control over particle size distributions to be exerted relative to typical conventional high surface area catalysts prepared by incipient wetness impregnation.

This study examines the CO + NO reaction over Pd by comparing kinetics data taken from conventional high surface area Pd/Al_2O_3 powder catalysts with kinetics and adsorption characteristics determined for CO + NO over planar model supported $Pd/Al_2O_3/Ta(110)$ catalysts and Pd single crystals. Such a combined approach exploits the complimentary nature of these three types of catalyst. Particle size dependencies on reaction activity that are evident for the supported catalysts are compared with analogous

0021-9517/97 $25.00

structural dependencies observed for different Pd single crystals (5, 6) and are related to the structure sensitive formation and stabilization of an atomic nitrogen species.

II. EXPERIMENTAL

The single-crystal and model planar-supported catalyst experiments were performed utilizing several combined UHV–microreactor systems previously described in the literature (23, 24) equipped with an array of modern surface characterization techniques including Auger electron spectroscopy (AES), X-ray photoelectron spectroscopy (XPS), *in situ* infrared reflection absorption spectroscopy (IRAS), and temperature-programmed desorption (TPD). Additionally, a gas chromatograph (GC) was incorporated into the gas handling system coupled with the microreactor for the analysis of product gases. A vacuum syringe, described in detail elsewhere (25), allows for a compression of the product gas into the sample loop, enhancing the amount of analyte, which is important in measuring the yield of the low surface area catalysts.

The planar-model-supported catalysts were obtained by vapor depositing Pd onto a previously prepared Al_2O_3 thin film supported on a Ta(110) substrate. The Pd was evaporated from a source comprised of a high-purity Pd wire tightly wrapped around a resistively heated Ta filament. The preparation of the Al_2O_3 thin film has been described previously (26). The sample temperature was monitored using a type "C" thermocouple junction spot-welded to the edge of the single-crystal substrate and the TPD experiments were carried out with a linear heating rate of 5 K/s.

In addition to these models supported on single crystals, special Pd/Al_2O_3 model catalysts supported on C films on Mo grids were prepared that were suitable for analysis by transmission electron microscopy (TEM). These samples were prepared by mounting thin carbon films (on the order of a few micrometers) onto Mo TEM grids and introducing them into UHV. Alumina films and Pd particles were deposited in exactly the same manner described above, providing model catalysts that could be imaged using TEM. The JEOL JEM 2010 model TEM was used for these studies.

The Pd/Al_2O_3 powder catalysts were prepared by a standard incipient wetness impregnation technique using a Pd nitrosyl nitrate solution. Three different loadings of Pd were added to a γ-Al_2O_3 powder (surface area $\sim$155 m^2/g) in weight percentages of 0.1, 1.0, and 5.0%. Additionally, a 2% Pd loading was added to a relatively low surface area α-Al_2O_3 support ($\sim$5 m^2/g). These choices of loadings and supports were made with the aim of achieving a wide range of average particle sizes. The dispersions and average particle sizes were determined using TEM and the rate of the $CO + O_2$ reaction as a measure of Pd surface area. This is described in detail elsewhere in the literature (27).

The kinetics experiments over the single-crystal and planar-model-supported catalysts were carried out in the UHV–microreactor systems in the batch mode using gas-phase IR spectroscopy and gas chromatography, respectively, to analyze products. The $CO + O_2$ and $CO + NO$ reactions over Pd/Al_2O_3 powders were performed in a conventional atmospheric flow reactor, composed of three Brooks 5850 mass flow controllers, a quartz microreactor tube housed in a ceramic heating furnace, and a Varian model 3400 GC, with a thermal conductivity detector. The GC column was the HayeSep DB (1/8 $\times$ 30 in.).

III. RESULTS AND DISCUSSION

TEM images for four different loadings of Pd in a planar-model-supported $Pd/Al_2O_3/C$ catalyst are presented in Fig. 1. The inset particle size histograms demonstrate the relatively uniform, narrow particle size distributions that can be obtained in the model catalysts prepared by this method. For the 10.0 ml Pd coverage the average particle size is $\sim$125 Å and the size distribution spans $\sim$200 Å. In contrast, the micrograph for the 5% Pd/γ-Al_2O_3 catalyst in Fig. 2, prepared by incipient wetness impregnation, reveals a similar average particle size, but shows a much wider range of particle sizes spanning $\sim$500 Å.

Kinetics studies on each of these three types of Pd catalysts reveal a distinct structure sensitivity. Figure 3 compares the $CO + NO$ Arrhenius plots for the model systems with those of the Pd/Al_2O_3 powder catalysts. The single-crystal and the planar-model catalyst reactions were carried out in the batch reaction mode at partial pressures of approximately 1 Torr in each reactant, while the powder catalyst data were acquired in the flow mode with CO and NO partial pressures of 4.5 and 5.2 Torr, respectively, in a He carrier gas. For the supported Pd/Al_2O_3 powder catalysts, a pronounced particle size dependence is clearly evident, with an increase in activity with increasing particle size. Likewise, larger particles in the model planar-supported catalyst display an activity enhancement over smaller ones, although the differences are not as pronounced as for the powders. A similar particle size dependence has been observed for supported Rh catalysts by Oh and Eickel (1). For the single crystals, the Pd(111) face exhibits a fivefold activity enhancement over the more open (100) and (110) faces.

Some differences are obvious at first glance. The single crystals exhibit higher activities and lower activation energies than do the powder catalysts. Table 1 compares these values among the different systems. This discrepancy between the single crystals and supported catalysts is not unique to Pd; similar findings have been reported for Rh catalysts (1, 28). As mentioned previously, the formation of an inactive atomic nitrogen species on low-coordinated defect sites has been suggested as a possible cause of this difference in behavior (1). However, this explanation does

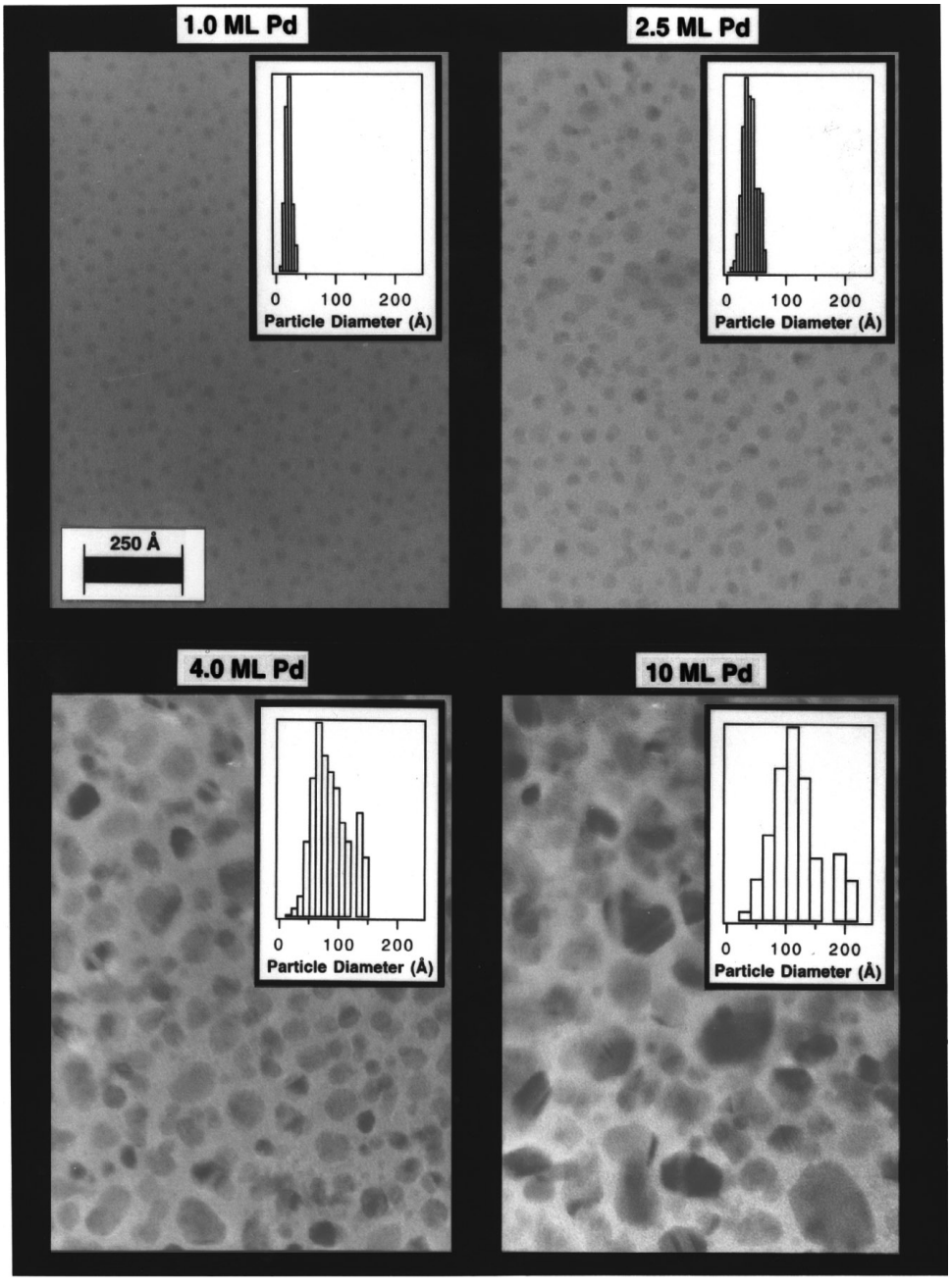

FIG. 1. TEM images of $Pd/Al_2O_3/C$ catalysts deposited at 500 K and annealed to 800 K for the indicated Pd coverages.

not address the differences in activity observed between the model particles and the powder catalysts. The origin of these differences is not clear at the present, but it should be noted that the activity data for these two types of catalysts were obtained in two different temperature regimes, due to practical experimental constraints (ensuring measurable product yields while avoiding gas phase mass transfer limitation over an adequate range of temperatures).

Despite these differences, there are also some intriguing correlations apparent among the activity trends observed in the three types of catalysts. Smaller particles, with their higher step/edge defect densities have more in common with the more open single crystal faces morphologically than do larger particles, while the larger particles have more (111) character relative to the smaller. This has been clearly illustrated by IRAS studies of model-supported Pd catalysts (30). Viewed from this perspective, the supported catalysts exhibit the same trend as the single crystals; open facets are less active than closed ones and small particles are less active than large ones. The origins of this structural

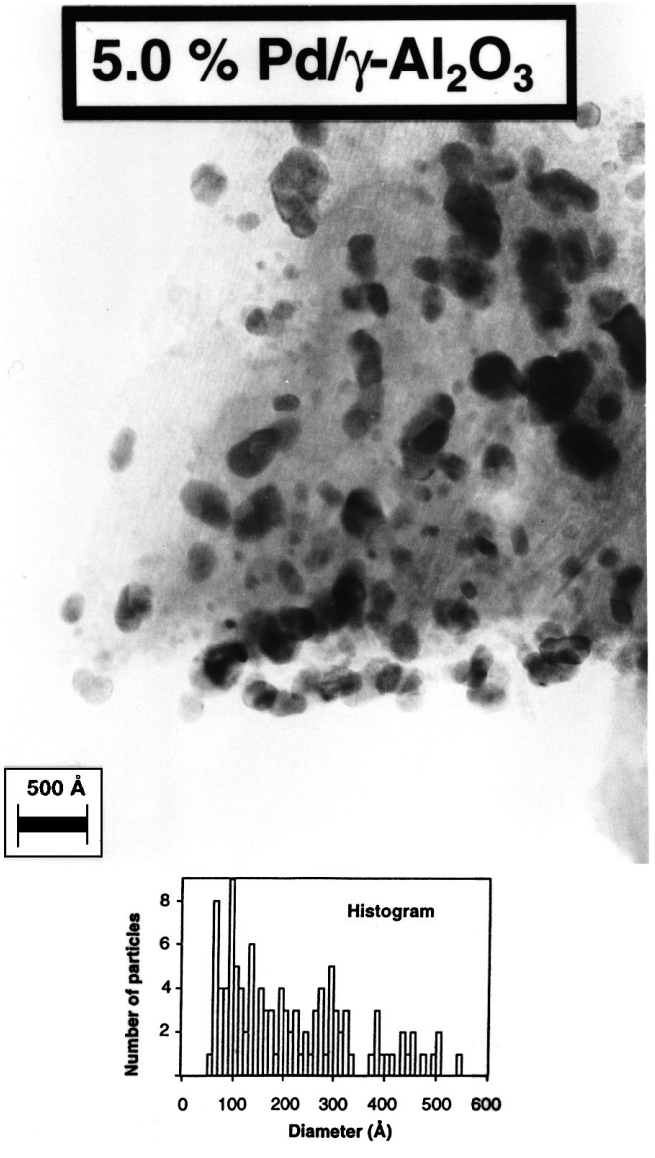

FIG. 2. TEM image and particle size histogram for a 5% Pd/γ-Al_2O_3 powder catalyst prepared by incipient wetness impregnation.

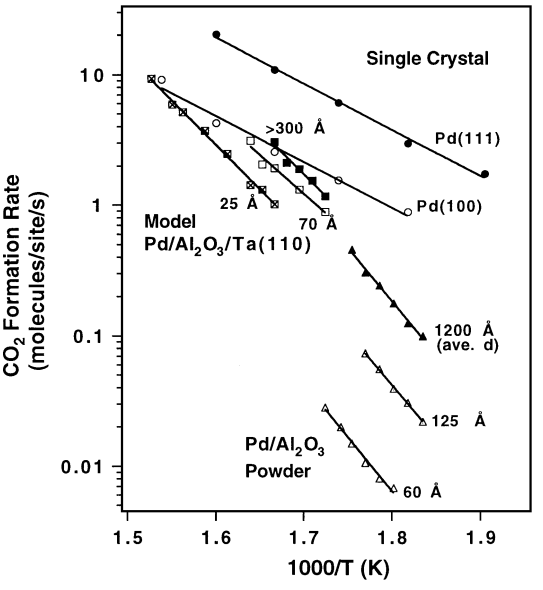

FIG. 3. CO + NO Arrhenius plots for single-crystal, model planar-supported, and Pd/Al_2O_3 powder catalysts. The powder catalyst data were taken in the flow reaction mode (4.4/5.2 Torr CO/NO ratio, steady state) and the model catalyst and single-crystal data were acquired for a batch reaction mode in 1 Torr of each reactant.

dependence have been investigated for the model catalyst systems. Two observations emerge that seem to provide some insight into this phenomenon.

First, the (111) facet stabilizes NO relative to CO at reaction temperatures to a greater degree than does the open (100) face. The relative ratio of adsorbed NO to adsorbed CO, estimated from IR absorbance intensities, is plotted as a function of surface temperature for the Pd(111) and (100) faces in Fig. 4. At CO + NO reaction temperatures, above 500 K, the ratio of adsorbed NO to CO on the (111) surface is on the order of 10 or more, while CO and NO populate the surface in roughly equal quantities at reaction temperatures for the (100) surface. An IRAS study of 500 Å Pd particles in a model $Pd/SiO_2/Mo(110)$ catalyst has indicated CO + NO coadsorption behavior very similar to that of the Pd(111) single crystal, with adsorbed NO being by far the dominant surface species at 500 K (30). There appears to be a correlation between the degree of stabilization of NO_a relative to CO_a on a particular surface at reaction temperatures, and the activity of that surface for the CO + NO reaction. The surfaces that exhibit the highest fraction of NO_a on the surface under reaction conditions also exhibit the highest activity for the reaction. This result is consistent with the observed reaction orders. Over the powder catalysts, the reaction was observed to be approximately

TABLE 1

CO + NO Reaction over Pd

	Approximate average particle size	Rate at 560 K (CO_2 formation TOF)	E_a (kcal/mol)
0.1% Pd/γ-Al_2O_3[a]	<30 Å	0.011	28.5
1.0% Pd/γ-Al_2O_3[a]	60 Å	0.007	37.6
5.0% Pd/γ-Al_2O_3[a]	125 Å	0.047	36.8
2.0% Pd/α-Al_2O_3[a]	1200 Å	0.22	37.3
Pd(0.6 ml)/Al_2O_3/Ta(110)[b]	25 Å	0.016[c]	27.4
Pd(5.5 ml)/Al_2O_3/Ta(110)[b]	70 Å	0.40[c]	28.2
Pd(35 ml)/Al_2O_3/Ta(110)[b]	>300 Å	0.53[c]	31.1
Pd(111)[b] [103]	—	4.2	16.2
Pd(100)[b] [103]	—	1.7	16.1
Pd(110)[b] [103]	—	1.1	17.0

[a] Flow reaction at 4.4 Torr CO, 5.2 Torr NO.
[b] Batch reaction at 1 Torr CO, 1 Torr NO.
[c] Extrapolated to 560 K.

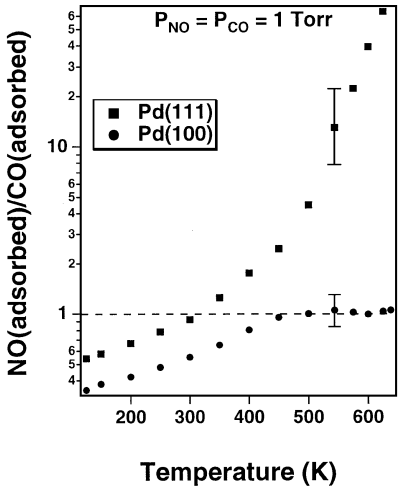

FIG. 4. The ratio of absorbed NO/CO based on IRAS intensity for Pd(111) and (100) as a function of temperature in 1 Torr of each gas.

positive one-half order in NO and negative first order in CO (27). Similar dependences were observed for the single crystals.

The second observation is that the more open surfaces promote the formation and/or stabilization of an inactive adsorbed nitrogen species. The series of TPD spectra in Fig. 5 shows the desorption behavior for ^{15}NO adsorbed on the Pd(111) and (100) surfaces at different substrate temperatures. The samples were exposed in a 1×10^{-5} Torr background pressure of ^{15}NO for 5 min at the indicated temperatures and then cooled in this background. Two recombinative $^{15}N_2$ desorption peaks attributed to atomic nitrogen are apparent for each surface. A low-temperature desorption feature with a peak maximum at 450 K appears on both substrates at every adsorption temperature, along with a high-temperature feature with a peak maximum between 545 and 626 K. The fact that the desorption temperature for the more strongly bound N_a is higher than the reaction temperatures employed in these studies suggests that this species is inactive at these temperatures. Figure 5 clearly indicates that the dissociation of NO and the stabilization of atomic nitrogen on Pd surfaces is structure sensitive. The total combined TPD peak areas of the two $^{15}N_a$ features at every temperature is larger for the (100) face, implying that this surface is the more active for NO dissociation. Additionally, the ratio of the concentration of the high-temperature (inactive) species to that of the low-temperature (active) species based on TPD peak area is higher for the (100) surface than for the (111) surface.

These results indicate that the dissociation of NO is not the rate-limiting step in this reaction over Pd, as has been suggested for Rh catalysts (31). The Pd(100) surface, more active for the dissociation of NO than Pd(111), exhibits the lower activity for the reaction. This correlation implies that the removal of the thermally stable atomic nitrogen is more important than NO dissociation in determining the kinetics of this reaction.

Similar results are obtained for the coadsorption of $CO + {}^{15}NO$ at a 1:1 ratio and total pressure 1×10^{-5} Torr (Fig. 6). Again, Pd(100) clearly displays a higher ratio of the inactive to active $^{15}N_a$ feature than does Pd(111). In order to quantify this, the TPD peak areas for the inactive $^{15}N_a$ on each surface were compared to that of a monolayer coverage of $^{15}N_a$ on Pd(100). This monolayer was obtained by reacting 1 Torr of ^{15}NO with 1 Torr of H_2 over Pd(100) at 550 K. Comparing the peak areas indicates that, after a 5-min exposure to CO + NO at 550 K, Pd(100) is 80% covered by the inactive N_a species, while Pd(111) is only 20% covered (6). This observation is consistent with the activity data. The (100) surface, more subject to poisoning by this inactive N_a species, exhibits the lower activity.

This enhancement for NO dissociation and stabilization on the more open face is also revealed by XPS study. After

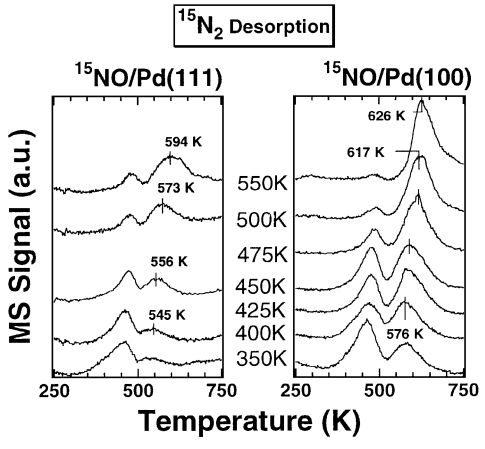

FIG. 5. TPD spectra for $^{15}N_2$ recombinative desorption after a 500-langmuir exposure to ^{15}NO at each of the indicated substrate temperatures on Pd(111) and (100).

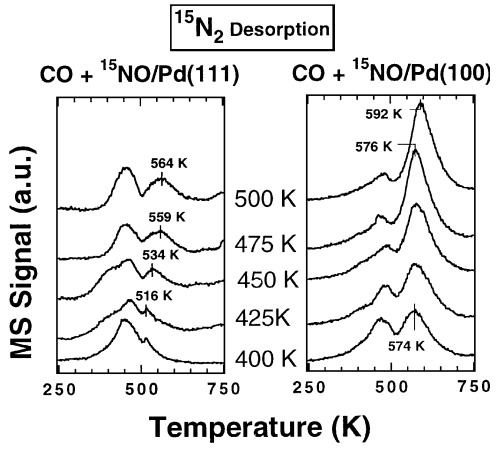

FIG. 6. TPD spectra for $^{15}N_2$ recombinative desorption after a 500-langmuir exposure to $^{15}NO + CO$ (1:1) at each of the indicated substrate temperatures on Pd(111) and (100).

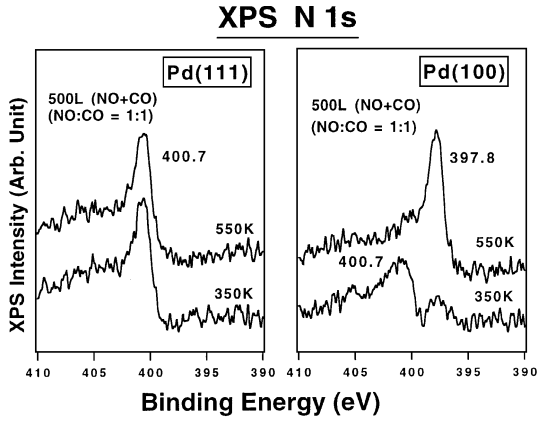

FIG. 7. XPS of the N1*s* peak on Pd(111) and (100) after a 500-langmuir exposure to CO + NO (1 : 1) at 350 K and 550 K.

a 500-langmuir exposure to a 1 : 1 mixture of CO + NO at 550 K and 1×10^{-6} Torr, followed by cooling to room temperature in the CO + NO background, significant differences are noted in the N1*s* XPS spectrum (Fig. 7) between the Pd(111) and (100) surfaces. The peak at 400.7 eV is attributed to N in an adsorbed NO molecule, while the feature at 397.8 is assigned to N_a. The N_a signal for the Pd(111) surface is beneath the detection limit, while this feature dominates the spectrum for the (100) surface. Even for the 350 K exposure temperature, a significant degree of NO dissociation has clearly occurred for Pd(100). The XPS annealing series in Fig. 8 demonstrates that the N_a species is stable up to surface temperatures of ~650 K, above which the N_a signal begins to significantly attenuate.

Referring again to the TPD data, coadsorption with other adsorbates (CO, NO, etc.) shifts the N_2 desorption peak maximum to lower temperatures. Comparing the TPD spectrum for the pure N_a monolayer on Pd(100) with those resulting from the CO + NO adsorption at 500 K reveals a 50 K difference in the desorption maximum for the Pd(100) and a 75 K difference for the Pd(111). This 25 K difference between the (100) and the (111) is another indication that the high-temperature N_2 desorption represents an inactive N_a species. At some critically high temperature, the CO + NO reaction over Pd undergoes an exponential rate increase that rapidly drives it to 100% conversion. At a 20 Torr total pressure of a 1 : 1 CO and NO mixture, this so called "light off" occurs at 625 K for Pd(111) and at 650 K for Pd(100) (6). This correlation between the differences for the two surfaces in the light off temperatures and the high-temperature N_2 desorption maxima is clearly suggestive that this stable N_a species inhibits the reaction. The correlation between the light off temperature on Pd(100) and the thermal stability of N_a on this surface as determined from the XPS annealing experiment (Fig. 8) should also be noted.

The NO adsorption behavior of Pd particles in model $Pd/Al_2O_3/Ta(110)$ systems as a function of particle size was investigated in a manner similar to that employed for the single crystals. The particles were exposed to a background pressure of 1×10^{-7} Torr ^{15}NO for 5 min at 550 K and then cooled to 350 K prior to ^{15}NO removal. The desorption spectra for $^{15}N_2$ and $^{15}N_2O$ over several different Pd loadings are presented in Fig. 9. The behavior is very similar to that of the single crystals. For recombinative $^{15}N_2$ desorption, a low-temperature feature is observed at ~520 K, along with a high-temperature feature above 600 K. The desorption temperature of the low-temperature feature is ~70 K higher than on the single crystals, consistent with having an increased concentration of strongly binding step/edge defect sites on the supported particles.

The spectra in Fig. 9a display the trend of an increased ratio of the low temperature N_a to the more thermally

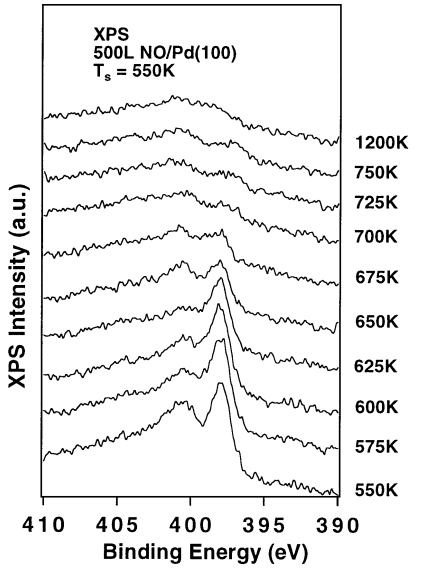

FIG. 8. XPS annealing series of the N1*s* peak on Pd(100) after a 500-langmuir NO exposure at 550 K.

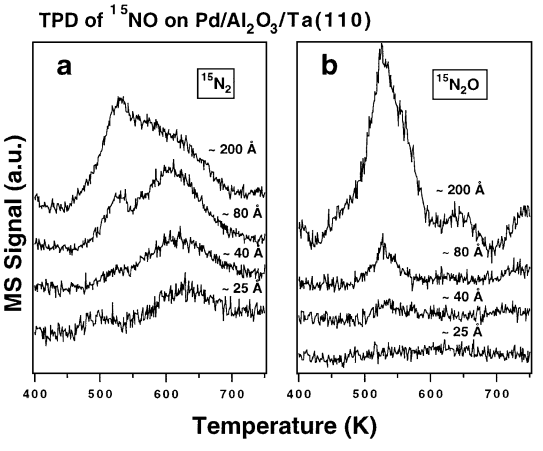

FIG. 9. TPD monitoring (a) $^{15}N_2$ desorption and (b) $^{15}N_2O$ desorption over several different Pd coverages with the indicated average particle sizes in a $Pd/Al_2O_3/Ta(110)$ catalyst after exposure to ^{15}NO at 550 K.

stable species (inactive N_a) with increasing particle size; also, the peak maximum of this inactive N_a feature is shifting to lower temperature. Again, this is what one might anticipate based on the morphology of the particles. The smaller particles with their higher percentage of surface defect sites stabilize the N_a to a greater degree than the large particles, as has been observed previously for Pd particles supported on Al_2O_3 (32).

Another observation apparent in Fig. 9b is that the larger particles are much more active for N_2O formation than the smaller ones. For the 20 Å particles in the 1.1-ml coverage, the amount of $^{15}N_2O$ desorption is beneath the detection limit. As the average particle size increases, an $^{15}N_2O$ desorption feature at ~530 K begins to grow in. For the 300 Å particles in the 22-ml loading, a large $^{15}N_2O$ desorption peak appears, with an integrated peak area approximately eight times larger than that of the 2.0-ml loading, though the total Pd surface area of the two catalysts differ by only just over a factor of 2. This enhancement for N_2O production with increasing particle size has been observed previously in TPD studies of Pd/SiO_2 model catalysts, for both NO adsorption and NO + CO coadsorption (33). This trend observed for the model supported catalyst in the low-pressure TPD experiment does not seem to extend into the high-pressure regime, as discussed below. The selectivity over the single crystals for the reaction at 1 Torr total pressure and a 1 : 1 CO/NO ratio is plotted versus reaction temperature in Fig. 10. The Pd(111) surface exhibits an enhancement for N_2O production relative to Pd(100) and (110). This is not surprising in light of the TPD results that show the more open (100) face to be more active for N_2 formation and stabilization than the (111). An increased coverage of atomic nitrogen on the surface would be expected to favor the formation of N_2.

The selectivities for the supported catalysts, both model and powder, are not as easily interpreted. No appreciable

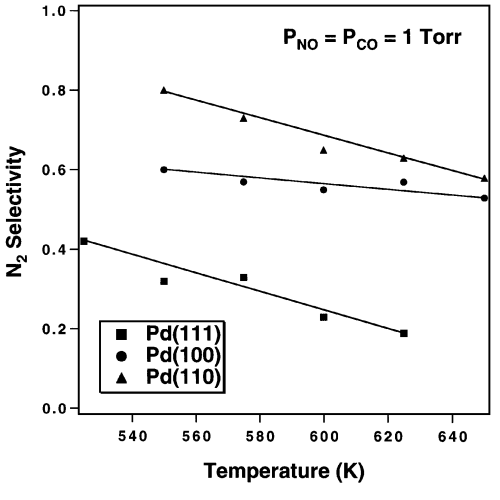

FIG. 10. N_2 selectivity vs temperature for Pd(111), (100), and (110).

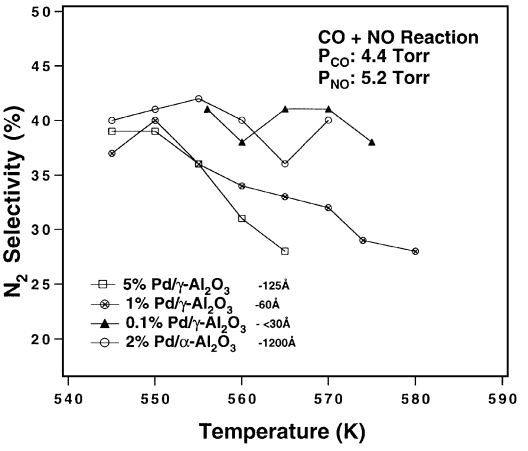

FIG. 11. N_2 selectivity vs temperature for the CO + NO reaction over each powder catalyst.

size dependence was observed for the powder catalysts (27) (Fig. 11) nor for the planar-model-supported catalysts. Although this is consistent with previous results reported for supported Rh catalysts, it represents somewhat of a discrepancy from the single crystal behavior. Because such a strong correlation exists for the observed structural dependencies for the absolute activity of the reaction between the supported catalysts and the single crystals, one might anticipate these similarities to be reflected in the selectivity behavior as well. If this were true, large particles would exhibit a stronger selectivity for N_2O production than smaller particles. As noted above, such an enhancement was observed in low-pressure TPD experiments for model-planar-supported Pd/Al_2O_3 and Pd/SiO_2 systems. However, for the high-pressure reaction (~1 Torr in each reactant), no such dependence is evident. The N_2O selectivity does not vary appreciably from the range 40 to 50% over the three planar-model-supported systems, though they span a significant range of particle sizes and display differences in overall activities.

The reasons behind the apparent absence of particle size dependence for selectivity in this reaction at the higher pressures for supported particles are unclear. It has been suggested that subtle changes in the stoichiometry of the reactant gas can have significant influences on the selectivity over Rh catalysts (33), and this possibility cannot be discounted for Pd. This problem warrants further study.

IV. CONCLUSIONS

To summarize, comparing the kinetics results for single-crystal and planar-supported model catalysts with those observed for conventional high-surface-area Pd powder catalysts reveals some intriguing correlations among these three types of systems. The particle size dependence for activity observed for the supported catalysts seems to reflect the

structure dependence displayed over different single crystal surfaces. TPD results of adsorbed NO and coadsorbed CO + NO on single-crystal and model-planar-supported catalysts indicate that the removal of an inactive atomic nitrogen species may be important in determining the activity. This is corroborated by XPS studies for the single crystals.

There are also some notable differences that emerge from this comparison. The energies of activation for the supported catalysts are significantly higher than those observed for the single crystals. There is also a discrepancy in the absolute rates, particularly between the powder catalysts and the single crystals, which is probably related to the high concentration of low-coordinated defect sites associated with small supported particles. This high concentration of undercoordinated sites on the supported particles results in a higher activity for forming and/or stabilizing certain inhibiting species on the surface, such as the inactive N_a species, which has been shown to be linked to open surfaces and low-coordinated defect sites. The dissociation of CO and subsequent carbon poisoning may also play an important role on the supported catalysts, something that would not be reflected in the single-crystal results.

ACKNOWLEDGMENTS

We acknowledge with pleasure the support of this work by the Department of Energy, Office of Basic Energy Sciences, Division of Chemical Sciences, and the Robert A. Welch Foundation.

REFERENCES

1. Oh, S. H., and Eickel, C. C., *J. Catal.* **128**, 526 (1991).
2. Oh, S. H., Fisher, G. B., Carpenter, J. E., and Goodman, D. W., *J. Catal.* **100**, 360 (1986).
3. Cho, B. K., *J. Catal.* **148**, 697 (1994).
4. Valden, M., Aaltonen, J., Kuusisto, E., Pessa, M., and Barnes, C. J., *Surf. Sci.* **307–309**, 193 (1994).
5. Vesecky, S. M., Chen, P. J., Xu, X., and Goodman, D. W., *J. Vac. Sci. Technol. A* **13**, 1539 (1995).
6. Vesecky, S. M., Rainer, D. R., and Goodman, D. W., *J. Vac. Sci. Technol. A*. **14**, 1457 (1996).
7. Schuth, F., and Wicke, E., *J. Phys. Chem*. **144**, 239 (1985).
8. Butler, J. D., and Davis, D. R., *J. Chem. Soc., Dalton Trans.* **21**, 2249 (1976).
9. Carballo, L. M., Hahn, T., and Lintz, H.-G., *Appl. Surf. Sci.* **40**, 53 (1989).
10. Hahn, T., and Lintz, H.-G., *Appl. Surf. Sci.* **40**, 59 (1989).
11. Ng, K. Y. Simon, Belton, D. N., Schmieg, S. J., and Fisher, G. B., *J. Catal.* **146**, 394 (1994).
12. Howitt, C., Pitchon, V., and Maire, G., *J. Catal.* **154**, 47 (1995).
13. Shelef, M., and Graham, G. W., *Catal. Rev.-Sci. Eng.* **36**, 433 (1994).
14. Taylor, K. C., *Catal Rev.-Sci. Eng.* **35**, 457 (1993).
15. Armor, J. N., *Appl. Catal. B: Environ.* **1**, 221 (1992).
16. Sault, A. G., and Goodman, D. W., *Adv. Chem. Phys.* **76**, 153 (1989).
17. Goodman, D. W., *Surf. Rev. Lett.* **2**, 9 (1995).
18. Goodman, D. W., *Surf. Sci.* **299/300**, 837 (1994).
19. Goodman, D. W., *Chem. Rev.* **95**, 523 (1995).
20. Poppa, H., *Vacuum* **34**, 1081 (1984).
21. Xu, X., and Goodman, D. W., *in* "Handbook of Surface Imaging and Visualization" (A. T. Hubbard, Ed.). CRC Press, Boca Raton, FL, 1995.
22. Rainer, D. R., Xu, C., and Goodman, D. W., submitted for publication.
23. Baetzold, R. C., and Hamilton, J. F., *Prog. Solid State Chem.* **15**, 1 (1983).
24. Hamilton, J. F., and Baetzold, R. C., *Science* **205**, 1213 (1979).
25. Vesecky, S. M., Rainer, D. R. and Goodman, D. W., submitted for publication.
26. Goodman, D. W., *Catal. Today* **12**, 189 (1992).
27. Rainer, D. R., Koranne, M., Vesecky, S. M., and Goodman, D. W., submitted for publication.
28. Cho, B. K., *J. Catal.* **131**, 74 (1991).
29. Rainer, D. R., Wu, M.-C., Mahon, D., and Goodman, D. W., *J. Vac. Sci. Technol. A*. **14**, 1184 (1996).
30. Xu, X., Chen, P. J., and Goodman, D. W., *J. Phys. Chem*. **98**, 9242 (1994).
31. Peden, C. H. F., Belton, D. N., and Schmieg, S. J., *J. Catal.* **155**, 204 (1995).
32. Cordatos, H., Bunluesin, T., and Gorte, R. J., *Surf. Sci.* **323**, 219 (1995).
33. Xu, X., and Goodman, D. W., *J. Phys. Chem*. **98**, 9242 (1994).